ACS APPLIED NANO MATERIALS

www.acsanm.org Article

3D Atomic Understanding of Functionalized Carbon Nanostructures for Energy Applications

Chilan Ngo,[#] Margaret A. Fitzgerald,[#] Michael J. Dzara, Matthew B Strand, David R. Diercks, and Svitlana Pylypenko*

Cite This: *ACS Appl. Nano Mater.* 2020, 3, 1600−1611 Read Online

ACCESS | Metrics & More | Article Recommendations | Supporting Information

ABSTRACT: Functionalized carbon nanostructures have garnered significant research interest as a class of materials for a myriad of energy applications, including fuel cell catalysts, and batteries. However, the design and optimization of these materials is impeded by the challenges in identifying heteroatom chemical speciation and spatial distribution within a carbon nanomaterial, as well as correlating these properties with application-specific performance metrics. In this work, a set of nitrogen-functionalized carbon nanospheres ($N-C_{sph}$) was synthesized with independent control over nitrogen functionality and $N-C_{sph}$ size and shape. This study features atom probe tomography (APT) of these isolated N-doped carbon nanospheres along with a thorough description of many considerations and challenges for APT of these materials, considering both sample preparation and analysis of data. The APT discussion provides a foundation for future studies of modified C materials with the goal of gaining insights into 3D heteroatom distribution within functionalized carbon nanomaterials through cross-correlative analysis between APT and complementary characterization techniques. Transmission electron microscopy (TEM), energy dispersive X-ray spectroscopy (EDS), and X-ray photoelectron spectroscopy (XPS) was conducted in order to verify the morphology of the $N-C_{sph}$, 2D spatial distribution of nitrogen heteroatoms, and the chemical distribution of nitrogen functionalities. Variable energy XPS was employed to characterize the depth dependence of chemical species' distribution, showing that certain nitrogen functionalities were more surface-enriched than others. This study discusses cross-correlative analysis between APT and XPS, with the two techniques providing powerful complementary elemental and chemical information for energy application materials.

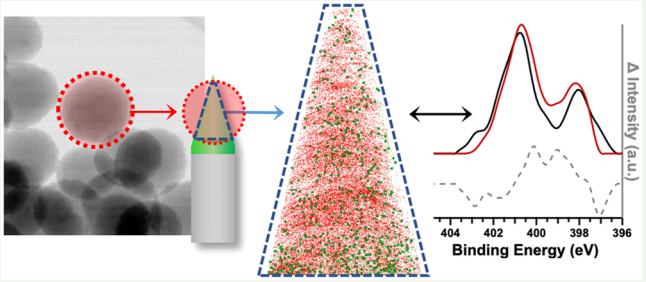

KEYWORDS: *N-doped carbon, atom probe tomography, X-ray photoelectron spectroscopy, heteroatom distribution, 3D reconstructions, energy materials*

INTRODUCTION

As energy demands continue to grow at a rapid pace, the development and improvement of renewable energy resources has become increasingly significant to the worldwide community. Carbon provides a flexible platform to fit a broad range of energy and environmental applications, as it is relatively inexpensive, abundant, and highly tunable with a myriad of allotropes/structures. Commonly utilized carbon-based materials span from traditional forms (e.g., graphite and carbon black), to more recently developed nanostructured materials (e.g., carbon nanotubes, graphene, and mesoporous carbons).[1−6] Within each class of carbon structures, the inherent material diversity can be further expanded to achieve desired properties and performance criteria by doping or functionalization with various heteroatoms or metal sites.[7−10]

Research on carbon functionalization has featured a variety of metals and nonmetal heteroatoms such as boron, nitrogen, phosphorus, and sulfur—either incorporated into the carbon structure or attached via covalent bond. Systems featuring carbon modified with a single type of heteroatom have been used in many applications, particularly catalysis for electrochemical systems, H_2 storage, CO_2 capture, and battery applications.[7,8] Chemical speciation and spatial distribution of heteroatoms within the carbon structure have been shown to greatly impact the ability of the structure to adsorb/desorb gases, catalyze reactions, and store/stabilize metal atoms/nanoparticles.[11−17] Heteroatom functionality, density, and location relative to each other are known to affect catalytic, electrochemical, and sorption properties.[18−22] The critical importance of understanding heteroatom distribution can be further explored through the example of single-site catalysts, which are produced by covalent tethering of the desired active

Received: December 3, 2019
Accepted: January 22, 2020
Published: January 22, 2020

https://dx.doi.org/10.1021/acsanm.9b02360
ACS Appl. Nano Mater. 2020, 3, 1600−1611

Scheme 1. Schematic of Synthesis, Sample Preparation, and Cross-Correlative Analysis of Functionalized Carbon Nanospheres Presented in This Study

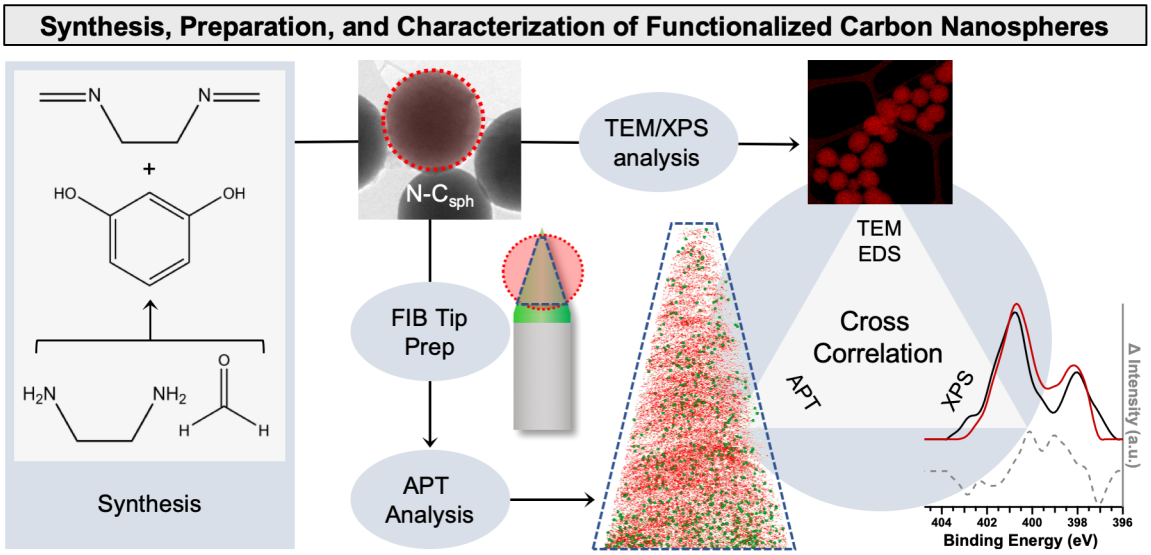

moiety to a functionalized carbon support, along with other synthetic schemes. In particular, nitrogen-modified carbons containing an atomically dispersed transition metal within a carbon network are promising for several important electrocatalytic reactions, including the oxygen reduction reaction for fuel cell systems. For this class of materials, crucial parameters to catalytic activity include coordination, relative distribution, and density of functional groups and metal sites.[23−25] These systems require fine control over both heteroatom and single-site metal distribution in order to produce the exact conditions/environments needed for catalysis.[26−28]

Although introducing heteroatom(s) and atomically dispersed metals has shown improved utility of various functional carbon structures, a central theme remains: the heterogeneous, complex nature of dopants sites within these materials clouds their understanding and further optimization. Difficulties are partially due to the complexity of the carbon structures being modified—different initial chemistry, structure, and morphology—and also the breadth of different approaches that are used to functionalize these carbons.[7,8] Synthetic methods include a variety of wet-chemical schemes, often with subsequent thermal treatment(s),[26,29−31] exposure to reactive gases,[13,14,32] and physical methods such as ion implantation.[33−35] Many of these processes impact the carbon matrix properties, in addition to the chemical/electronic modification that occurs from heteroatom incorporation. To move toward rational design based on tuning the properties desired for a particular application, it is imperative to better control heteroatom chemistry and distribution, while either minimizing or directing the changes in carbon structure.

Significant efforts have been dedicated to determine the physical and chemical properties of functionalized carbon using a variety of characterization techniques, including physisorption and chemisorption techniques, Raman and infrared spectroscopies, X-ray photoelectron spectroscopy (XPS), transmission electron microscopy (TEM), scanning TEM (STEM) coupled with energy dispersive X-ray spectroscopy (EDS), and electron energy loss spectroscopy (EELS).[7,8,36] Despite the strength of these methods, understanding of the chemical speciation, elemental distribution, and morphological properties across micro/nano/subnano length scales, spatial area, and depth is still limited. Moreover, chemical information obtained with the aforementioned techniques is often averaged over relatively large areas, while elemental distributions lack identification of chemical speciation and are generally limited to 2D inspection. Insights remain largely unexplored for atomic-level composition, information on 3D distribution of dopants, and the subsequent impact on application-driven properties.

To fill this gap, we turn to atom probe tomography (APT), a technique with the potential to provide highly detailed analysis, but has yet to be explored for this class of materials. Invented about 50 years ago,[37] APT has been progressively developed into a method capable of providing 3D, atomic reconstructions of materials with high compositional sensitivity (ppm) and spatial resolution (~0.2 nm). The technique is based on layer-by-layer field evaporation of material from a sharp tip; 2D position- and time-sensitive detection of ionic species via time-of-flight mass spectrometry provides 3D information on the original atomic positions and atomic identities. APT is most commonly performed on specimens prepared from bulk metals and alloys, followed by bulk and thin film dielectrics.[38] More recent studies have explored APT of semiconductor materials and related devices, as well as various fields including batteries, geological and biomineralized materials, ceramics, nanoscale particles or features within a bulk matrix, and fully organic molecules.[38−40] Of particular relevance to this paper is work showing dopant distributions in semiconducting nanowires[41−43] and fresh/spent zeolite catalysts,[44−46] as our goal is to identify precise atomic distributions and possible clustering of heteroatoms that can then be correlated with performance characteristics (catalytic activity, sorption properties, etc.).

For evaluation in the atom probe, material of the correct morphology and composition must be fabricated as a thin, sharp tip (<300 nm diameter), a possibility that is provided by focused ion beam and scanning electron microscopy (FIB/SEM) systems. The size and dimensions of the nanomaterial sample to be manipulated for atom probe analysis significantly affects the preparation method used in the FIB system. For

https://dx.doi.org/10.1021/acsanm.9b02360
ACS Appl. Nano Mater. 2020, 3, 1600−1611

example, small nanoparticles (5−50 nm) make it possible for multiple samples to fit in a tip using typical bulk preparation methods.[47−50] Nanowires can be manipulated or cut individually and adhered directly to a post.[51] However, nanomaterials in the 50−200 nm range require further considerations to prepare, which is one of the main reasons that APT studies of the carbon-based structures typically used in sorption and catalytic applications have not yet been reported in the literature.[52]

To aid in proof of principle APT studies, it is critical to compliment and corroborate APT data with other characterization methods. XPS is widely used to provide near-surface information on the relative abundance of different elements and their chemical/bonding state.[53] The utility of XPS can be expanded through variable energy excitation using synchrotron sources. Surface sensitivity of XPS is primarily a function of the inelastic mean free path (IMFP) of the ejected photoelectrons contributing to the measured signal, which in turn depends on the kinetic energy (KE) of the ejected photoelectron.[53,54] The KE of an electron ejected from a given core level can be controlled by varying the incident photon energy ($h\nu$), therefore enabling depth profiling on nonuniform samples for which conducting traditional angle-resolved XPS would be problematic. Variable energy XPS quantifies the relative abundance of chemical species at depths on the order of 1−10 nm, critical data for validating APT reconstructions. In turn, through APT reconstructions and cluster analysis, identifying which species are most abundant on the surface enables refinement of XPS fitting and assignment of components to physical species. By corroborating and contrasting depth-resolved chemical speciation, both APT and XPS data can be presented with greater confidence.

Here, we provide a first step toward true 3D, atomistic understanding of functionalized carbon-nanostructures using nitrogen-functionalized carbons (N−Cs) as the initial system. Scheme 1 demonstrates the steps outlined in this study. Spherical N−C particles (N−C_{sph}) prepared by a solvothermal treatment and pyrolysis procedure adapted from the literature[55] were selected due to the ability to independently modify both morphological and chemical properties of these materials, through the control of different synthetic variables. An array of sizes with different relative abundances of N−C chemistries was synthesized to fit into dimensions suitable to APT analysis. XPS was used as a starting point to assess the gradient in nitrogen speciation present in these samples. This was accomplished by using two different photon energies to change information depth. Next, initial results and challenges of APT toward these materials are discussed, along with solutions through either present or potential future work. Ultimately, this work demonstrates the potential of APT in conjunction with variable energy XPS in multitechnique studies of functionalized carbon structures, specifically to associate the interplay of heteroatom distribution and chemistry with physicochemical properties and applicability.

EXPERIMENTAL SECTION

Solvothermal Synthesis of N−C_{sph}. The preparation of N−C_{sph} was modified from a previously reported sol−gel synthesis.[55] Initially, 3.2 g of resorcinol (Sigma-Aldrich, >99%) was dissolved in an aqueous alcohol solution prepared from 320 mL of H_2O (18.2 MΩ) and 128 mL of ethanol (Pharmco-Aaper, 200 proof absolute anhydrous) in a 1 L HDPE screwcap bottle while stirring at 300 rpm. A variable volume of ethylenediamine (EDA, Sigma-Aldrich, >99.5%) was added while stirring, followed by 4.8 mL of formaldehyde (Alfa Aesar, 37 wt %). In this work, EDA volumes of 3.2 mL, 4.8 mL, 5.4 mL, and 6.0 mL correspond to 0.70%, 1.05%, 1.18%, and 1.31% of total solution volume, respectively.

After 24 h, stirring was discontinued and the bottle was sealed with DuraFilm prior to heating at 100 °C for another 24 h. Following hydrothermal treatment, the bottle was cooled under running tap water, and polymerized spheres (PS) were isolated by centrifugation of the reaction mixture at 9000 rpm (9327*g*) in a Marathon 22kbr centrifuge for 20 min. The product was then dispersed in ethanol, transferred into quartz boats, and air-dried at 70 °C for 12 h to drive off ethanol. The PS were then pulverized into a fine powder via mortar and pestle, then pyrolyzed at variable temperatures under N_2 (General Air, UHP) flowing at 100 sccm. A quartz boat containing the PS was heated at 2 °C/min to 350 °C, held for 4 h, then heated at 5 °C/min to 600, 700, 800, or 900 °C. After dwelling for 2 h, the oven was allowed to cool to at least 100 °C prior to removal of the final N−C_{sph} product. While samples with the most differences in properties are shown in the paper, full analysis of all other samples can be found within the SI (Figures S1,S2, Tables S1−S3).

Electron Microscopy and Spectroscopy. Samples were prepared for electron microscopy by dispersing 0.1 mg of N−C_{sph} in 1 mL of ethanol and sonicating the mixture for 10 min, then dropping 5 μL of the solution onto a 300-mesh copper grid with lacey carbon backing (Ted Pella, 01895). Excess solution was removed after 15 s, and the grid was allowed to dry. Electron microscopy images were taken for screening (Philips CM200 TEM) and higher resolution analysis (FEI Talos F200X STEM) coupled with elemental mapping via EDS (acquisition time 10 min) was performed.

X-ray Photoelectron Spectroscopy. XPS was performed (Kratos AXIS Nova photoelectron spectrometer) using a monochromatic Al Kα source operating at 300 W with a photon energy of 1486.6 eV. Survey and high-resolution spectra (C 1s, O 1s, and N 1s) were acquired at 2×10^{-9} Torr operating pressure at pass energies of 160 and 20 eV, respectively. Samples were mounted on conductive carbon tape such that charge neutralization and charge referencing was not necessary. Typically, two or three spots on each sample were measured, and any quantification reported was an average of those values. XPS data were processed (CasaXPS software) using a linear background subtraction for quantification of C 1s, O 1s, and N 1s. Peak fitting was performed by a least-squares method using a series of components with a 70% Gaussian, 30% Lorentzian line shape. Components were fit to all N 1s spectra using a full width at half-maximum (fwhm) of 1.0 eV.

For XPS with increased surface sensitivity, XPS was also conducted at the Advanced Light Source (ALS) end-station 9.3.2.[56] Measurements of the N 1s were performed with a photon energy of 630 eV and a pass energy of 50 eV at a pressure of $\sim 5 \times 10^{-9}$ Torr. Spectra were normalized by total area to account for the differences in intensity between data collected on the two different instruments when calculating difference spectra.

Focused Ion Beam Milling. To produce APT samples of appropriate size and shape, a small, sharp tip must be milled from the material of interest via focused ion beam (FIB) milling, as is common for the current state-of-the-art methods for APT sample preparation. Prior to milling in the FIB, small wafers of silicon or gallium arsenide substrate were prepared by cleaving (as-needed) and cleaning by sonication in isopropyl alcohol, ethanol, and acetone. Substrates were then sputtered with gold on the polished surface using a Hummer VI sputtering system to apply an approximately 100 nm-thick layer of gold. Coatings over 100 nm thick were more prone to delamination from the substrate during FIB milling, so <100 nm bottom coatings were preferred. N−C_{sph} were dispersed in ethanol to obtain a 0.2 mg/mL sample solution, of which a 5 μL aliquot of solution was spin-coated onto the gold coated wafer at 2000 rpm for 4 min. Finally, a thicker layer of gold was sputtered onto the wafer for 15 min to coat the top of the spheres.

A FIB/SEM (FEI Helios NanoLab 600i) equipped with an Omniprobe Autoprobe 250 nanomanipulator needle and source for platinum deposition was used for the general tip-shaping procedure.

https://dx.doi.org/10.1021/acsanm.9b02360
ACS Appl. Nano Mater. 2020, 3, 1600−1611

Details of the extensive process are reported in the Supporting Information, with major steps summarized later in this text, as well as in Table S3.

Hummingbird Scientific holders were used to support the FIB-prepared samples, for their design compatible with FIB/SEM stages, Hummingbird TEM single-tilt holders, and sample pucks for Cameca Local Electrode Atom Probe (LEAP) instruments, allowing multi-technique characterization without moving or reloading the delicate samples.[57] Elemental composition, morphology, and initial screening of each sharpened tip was determined via TEM/EDS. Once TEM/EDS confirmed appropriate tip shape and size with a minimal amount of FIB-deposited platinum remaining, and sufficient N−C_{sph} material encapsulated, the holder was mounted onto an APT puck and loaded into the instrument chamber.

Atom Probe Tomography. APT was performed on a Cameca LEAP 4000X Si instrument, equipped with a 355 nm laser and straight flight path set to 90 mm. Data was collected in laser pulse mode (40 pJ, 333 kHz), with a base temperature set point of 55 K and detection rate of 3 to 5 ions per 1000 pulses. Processing and reconstructions were done via Cameca's IVAS 3.6.6 software. Original tip profiles were determined from TEM images. Detection efficiency (DE) and image compression factor (ICF) values were adjusted in order to produce 3D reconstructions more comparable to morphologies observed in the TEM images (see Supporting Information for specific parameters of each sample discussed in this paper). Tip shapes after destructive APT processing were also determined via STEM, in order to better estimate evaluation depth and assist in subsequent reconstructions. Because of the unknown bonding and atomic volumes of N−C_{sph} explored in this work, carbon density was maintained at the default value in IVAS (0.008785 nm^3/atom). For the presentation of reconstructions, iso-concentration surfaces are set at percentages representing elemental distribution based on each sample's corresponding STEM/EDS data, with volume filling of higher atomic concentration.

RESULTS AND DISCUSSION

Initial Characterization. *Proof of Principle: APT of N−C_{sph} and Complementary Characterization.* Comprehensive, multitechnique studies featuring APT are desired to obtain better understanding of surface vs bulk heteroatom distribution within functionalized carbon, with the eventual goal of visualizing the 3D distributions of heteroatoms and their chemical speciation. To demonstrate the viability of APT on N−Cs, a suitable N−C material series with controlled morphology and varied chemistry is needed for proof of principle studies. The preparation of APT tips requires careful consideration of the size and shape of the N−C nanomaterials, narrowing the field of suitable structures. Wickramaratne et al. have shown that N−Cs with spherical shape can be prepared by controlling the concentration of base present during the preparation of a resorcinol−formaldehyde solution, which inversely affects the size of the N−C_{sph} produced, as well as the amount of incorporated nitrogen.[55] Our study utilizes N−C_{sph} prepared in a similar fashion, initially using the largest volume of EDA reported by Wickramarante, and thus the smallest diameter (<100 nm) particles. These conditions were selected due to the expectation that smaller sizes provide higher probability of an APT data set containing both N−C_{sph} surface and bulk. Samples of specific shape and size were pyrolyzed from 600 °C up to 900 °C in 100 °C increments in order to vary both the nitrogen amount and the relative abundance of nitrogen heteroatoms. The temperature of pyrolysis impacts the concentration and functionality of nitrogen and the overall composition, as has been shown previously on similar materials.[23,58,59] For the sake of brevity, only the samples at extreme pyrolyzation temperatures of 600 and 900 °C are discussed in this paper. Additional information including TEM, STEM, and XPS on the intermediate samples are reported in the Supporting Information (Figures S1,S2, Tables S1−S3).

Electron Microscopy of N−C_{sph}. Samples pyrolyzed at 900 °C, shown in Figure 1a, demonstrate typical morphology and textures of the synthesized N−C_{sph}. Different TEM imaging modes highlight different visual features, notably with traditional bright field (BF) TEM having the highest resolution and showing sharper, subtle edges with ∼15 nm surface structures, and high angle annular dark field (HAADF) STEM producing a 3D-like image of surface topography and providing compositional information (Figure 1b). To evaluate the spatial distribution of nitrogen within the N−C_{sph}, EDS mapping was performed on the selected pyrolyzed N−C_{sph} samples (Figure 1). Elemental mapping for each sample visually suggests that all elements are homogeneously dispersed throughout the N−C_{sph}, with no evidence of differences between surface and bulk distribution of nitrogen species in N−C_{sph} samples pyrolyzed at 600 and 900 °C (including at higher magnifications than shown in Figure 1).

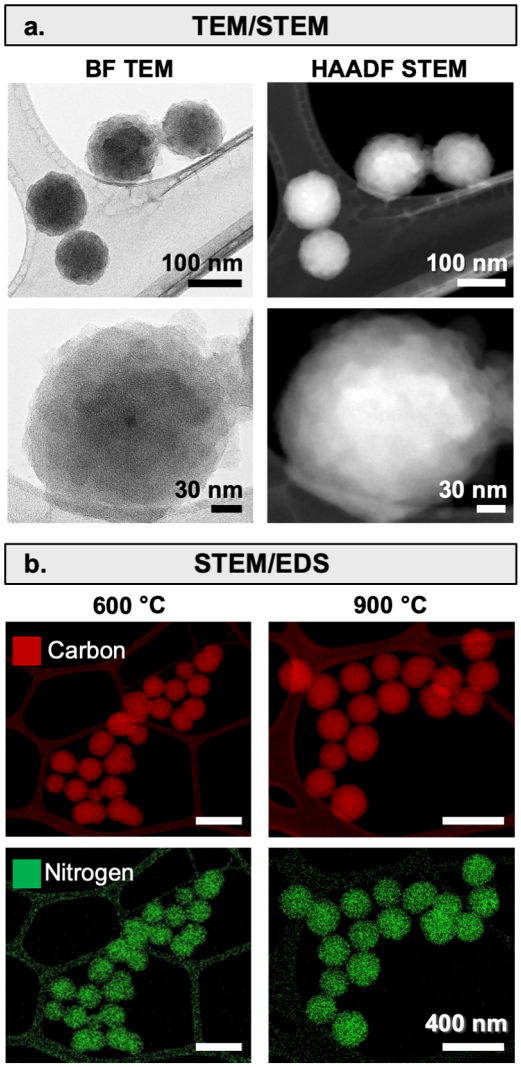

Figure 1. (a) High magnification TEM/STEM images of N−C_{sph} pyrolyzed at 900 °C show morphology/topography of N−C_{sph}. (b) Elemental mapping of 600 and 900 °C pyrolyzed samples from EDS in STEM mode display the spatial distributions of each element.

https://dx.doi.org/10.1021/acsanm.9b02360
ACS Appl. Nano Mater. 2020, 3, 1600−1611

Elemental Quantification: EDS and XPS. While results from EDS and XPS are both semiquantitative and derived from different volumes of material by nature, both techniques show a decrease of both oxygen and nitrogen content with increased pyrolyzation temperatures. In general, values for nitrogen are similar for the two techniques, suggesting that nitrogen is present in both the bulk and surface of the materials. As can be seen in Table 1, a slightly higher amount of oxygen and nitrogen is detected with XPS, however, suggesting enrichment of those elements at the surface of the N−C_{sph}. For oxygen this is consistent with expectations, as XPS measurements are more sensitive to possible contaminations such as adsorbed water, carbon dioxide, and oxygen-containing adventitious carbon. With respect to nitrogen, slight surface enrichment suggests that there may be depth-dependent differences in dopant distribution, which motivates further characterization probing composition at different depths.

Table 1. Elemental Composition from STEM/EDS and XPS Are Compared for Pyrolysis Temperatures of 600 and 900 °C. XPS Percentages Are Determined from C 1s, O 1s, and N 1s Spectra of the N−C_{sph}

atom %	600 °C		900 °C	
element	STEM/EDS	XPS	STEM/EDS	XPS
C	94.7	92.4	96.4	94.9
N	3.2	4.1	2	3.1
O	2.1	3.4	1.6	2.0

Surface Composition: XPS. Curve fitting of the N 1s was performed by application of a fit containing up to nine components to the N 1s of N−C_{sph} (Figure 2a,b). The components' fwhm values were rigidly constrained to 1.0 eV, while their positions were allowed to vary up to 0.2 eV for internal peaks, and up to 0.3 eV for the highest and lowest BE peaks where there is more variation from sample to sample, and a lower signal-to-noise ratio. Parameters for all components and samples are provided in Table S3, along with a detailed discussion of the rationale behind the assignment of physical species to components, which is based on a combination of our prior experience analyzing N−C materials and literature encompassing experimental and theoretical studies on a variety of N−C materials.[15,30,35,59−62] Variation in pyrolyzation temperature results in a noticeable change in the relative composition of the N−C_{sph} samples. The overall loss of nitrogen with increasing pyrolyzation temperature is accompanied by a decrease in all of the species occurring between 397.9 and 400.1 eV, corresponding to imine, pyridine, amine, and pyrrolic species. In contrast, a relative increase in abundance was observed for the in-plane H-pyridine species and the low-order graphitic nitrogen species.

To investigate the depth dependence of the distribution of nitrogen species within the set of N−C_{sph}, the N 1s of all samples were also measured using a synchrotron X-ray source with a $h\nu$ of 630 eV at the ALS end-station 9.3.2 (Figure 2c,d).[56] The decrease in $h\nu$ results in a kinetic energy (KE) of ejected N 1s photoelectrons of ∼230 eV, nearly 5× lower than the KE of the Al Kα X-ray source data (∼1080 eV). While a 5× difference in KE does not necessarily result in a 5× difference in information depth, it is appropriate to assume that the synchrotron data are more surface sensitive than data obtained with the Al Kα source. Background-subtracted data from each photon source was normalized by total region area—a necessary step to accurately compare data with significantly different intensities, due to the much higher flux of synchrotron sources over that of laboratory instruments. Difference spectra were produced by subtracting the data collected at 1486.6 eV from the data collected at 630 eV (Figure 2, dashed lines); positive features correspond to near-surface species and negative designated subsurface species. Visualizing the data in this manner allows for quick analysis of major trends while preserving absolute differences. The N−C_{sph} pyrolyzed at 600 °C show two main near-surface rich peaks at 397.5 eV and 399.5−400 eV, while the 900 °C sample has a broad near-surface rich regime from 398−401 eV. The 600 °C sample has a negative peak at ∼398.5 eV, indicating less pyridine in the near-surface, while 900 °C has a lower concentration of near-surface N-rich and edge H-pyridine species. Both samples show less graphitic nitrogen in the near-surface. The differences observed in the distribution of nitrogen species with change in information depth from XPS and the dependence of the nitrogen distribution on pyrolysis temperature during synthesis both motivate further study with APT, among other techniques, to better understand the nitrogen distribution on the surface versus that of the bulk.

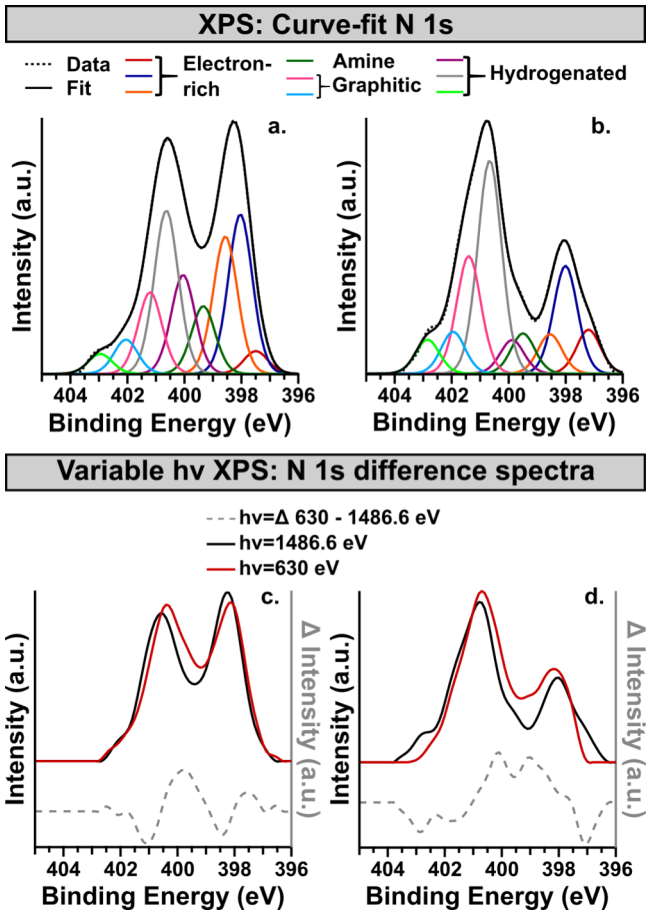

Figure 2. Relative abundance of nitrogen species in N−C_{sph} is evaluated by curve-fitting, applied to samples pyrolyzed at 600 °C (a) and 900 °C (b). Overlaid data and difference spectra are displayed for samples pyrolyzed at 600 °C (c) and 900 °C (d), such that a positive difference peak indicates a surface-rich species.

Proof of Principle: Initial APT Results. *APT: Preparation of N−C_{sph} Specimens by FIB.* To begin the APT sample preparation for nanospheres, first it is necessary to encapsulate N−C_{sph} with a protective layer of metal to preserve the

https://dx.doi.org/10.1021/acsanm.9b02360
ACS Appl. Nano Mater. 2020, 3, 1600−1611

surfaces from damage during the preparation of the tips for APT. A silicon wafer substrate was initially chosen to host the metal-encapsulated N−C_{sph} particles. A layer of metal was deposited directly onto the wafer, and a suspension of nanoparticles was spin-coated onto the metal-coated substrate. Next, nanoparticles were encapsulated with metal by depositing a second layer of metal onto the spin-coated sample (see Figure 3i−1). The initial substrate material used for this procedure was silicon and the encapsulating metal was copper; however, both of these material selections were further optimized to reduce special aberrations that result from uneven field evaporation. Procedural modifications such as these are discussed thoroughly in a later section.

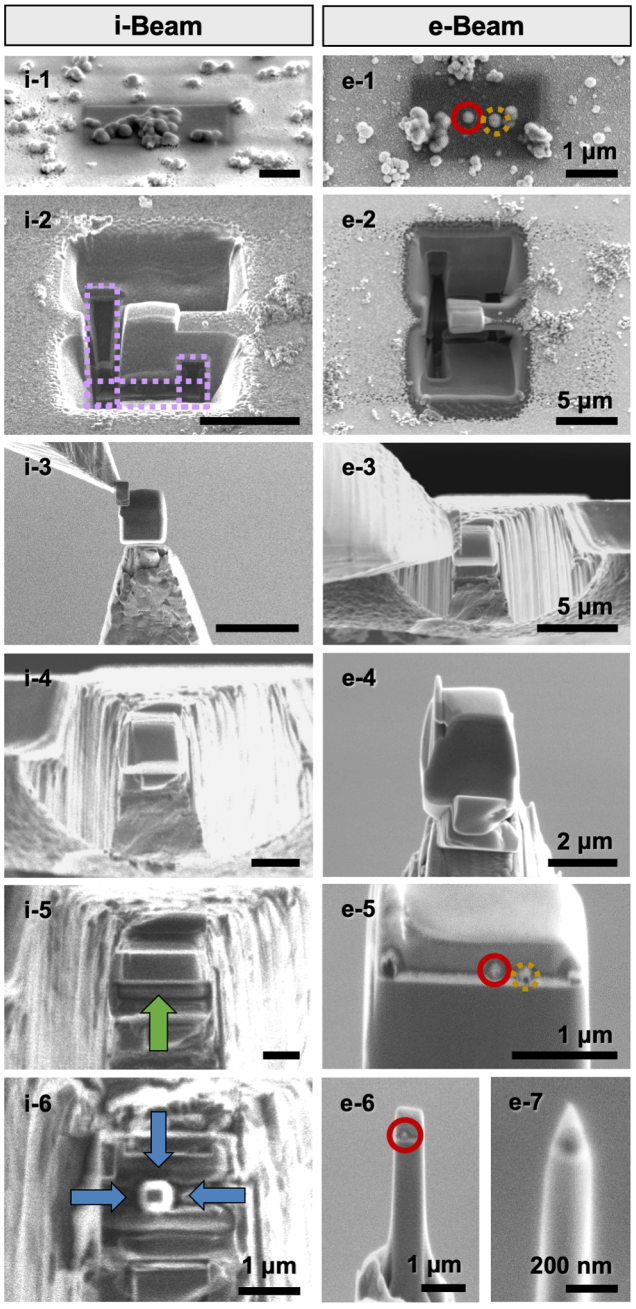

Figure 3. Summary of main FIB steps for APT sample preparation of single C nanospheres, as viewed in the ion beam (i-#) and electron beam (e-#). Note that for clarity, images may be from different samples. All image pairs are taken from the same stage tilt and similar magnifications, with subsequent viewing angles of 0° and 52°.

After encapsulation of N−C_{sph} on the substrate, the APT sample tip was prepared using an altered FIB-liftout method. A number of general steps are summarized in Figure 3: (1) Protecting the surface with a sacrificial cap of deposited Pt, (2) creating a rough slice of material by milling two parallel trench cuts around the protected area, then making a U-shaped cut perpendicular to them, (3) lifting the slice by attachment of one end to a sharpened manipulator and cutting the opposite end away, (4) attaching the slice to an APT sample post, (5) thinning the side facing the e-beam until a single particle of the targeted N−C_{sph} can be pinpointed, (6) milling the three remaining sides to create a square post with the nanosphere inside (blue arrows), and (7) final thinning of the post until the Pt coating is removed and the tip is sharp, while leaving the nanosphere sufficiently intact near the top of the sharpened area. Specific details of each step, and further considerations for FIB sample preparation are reported in the Supporting Information (Table S3).

APT: Cross-Correlative Tip Analysis. An inherent, continuing challenge of APT is the accuracy of generated reconstructions. Therefore, in this case, cross-correlative TEM imaging and EDS mapping are vital complementary steps after FIB/SEM tip preparation (Figure S4).[38,51,57,63,64] It is critical to evaluate every sample tip before the destructive APT process, not only because initial morphology is necessary information toward data reconstruction, but also because the general suitability of the specimen for APT analysis can be assessed. The desired particle may not be situated properly. For the goal of comparing dopant distribution on the surface versus bulk, the N−C_{sph} particle should be positioned such that the surface can be captured; each tip ideally contains both the bulk/inside and the surface/edge of a nanosphere. Because of resolution limits in the FIB/SEM as the specimen becomes smaller during milling, as well as the uncontrolled nature of milling during top-down sharpening, there is a degree of estimation and chance during the final thinning steps. To assist with determining spatial locations of elements and their relative compositions through APT, STEM/EDS was done in each complete tip. Initial APT results on a N−C_{sph} sample pyrolyzed at 600 °C (Figure 4) highlight the importance of cross-correlation. Here, 2D data show the projection of a single N−C_{sph} particle centered in a tip; however, rotated and tilted 3D reconstructions reveal two N−C_{sph} partially embedded in the sample.

While inadvertent, capturing two spheres in one tip allows for comparison between the N−C_{sph} analyzed with identical experimental conditions. Both the isoconcentration (iso) surfaces and point reconstructions show moderately homogeneous distributions of nitrogen in each particle section. This preliminary result demonstrates the feasibility of characterizing 3D heteroatom distribution of a single N−C_{sph} particle using APT. However, the shapes of the carbon iso surfaces suggest that aberrations do exist in the presented data. From the shape of the carbon iso surfaces it can be inferred that as the sample was partially evaporated, the carbon spheres might have ejected off of the tip, which then left only copper below the sphere to be evaporated and detected underneath the carbon. This would explain the semicircular shape seen in the APT data for which the TEM imaging displays an entire sphere in the sample. As expected for an emerging technique, improve-

https://dx.doi.org/10.1021/acsanm.9b02360
ACS Appl. Nano Mater. 2020, 3, 1600−1611

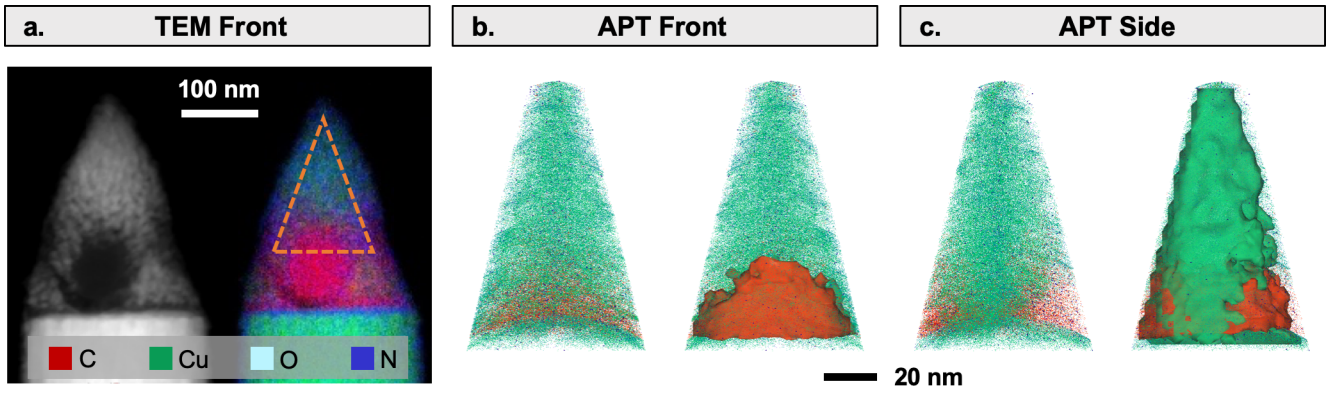

Figure 4. Initial APT reconstructions of Cu-encapsulated C nanospheres. (a) Initial STEM/EDS images of the sample tip. The orange triangle represents the volume that is thought to be represented by the atom probe reconstructions in panels b and c. (b) Front view of point distribution for C (red), Cu (cyan), and N (blue) along with an iso surface for C (5%); (c) Side view of point distributions and iso surfaces in panel b after *z*-axis rotation to show both particles. Reconstruction parameters can be found in the Supporting Information (Figures S4 and S5).

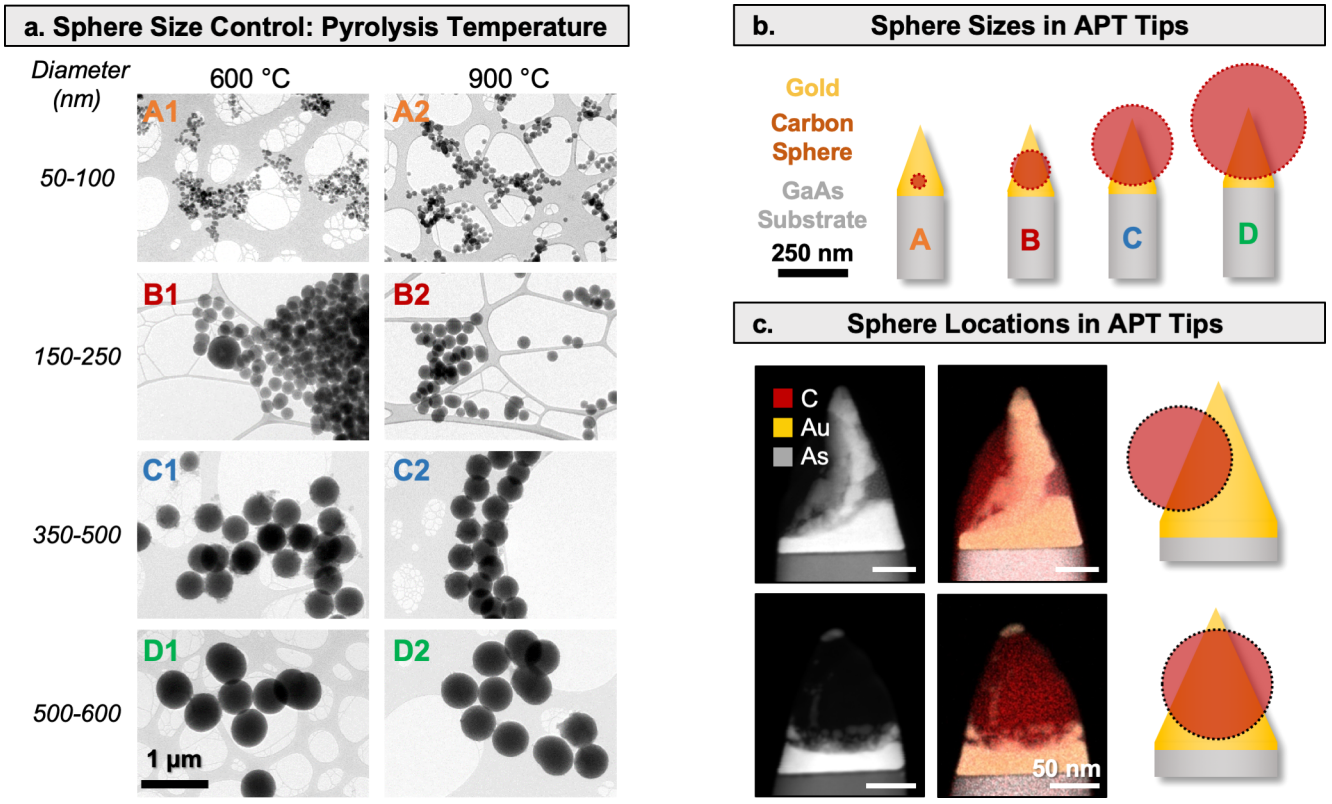

Figure 5. (a) Bright field TEM images of N−C_{sph} after pyrolyzation in flowing N_2 for samples prepared with decreasing amounts of EDA, (A) 1.31 vol %, (B) 1.18 vol %, (C) 1.05 vol %, (D) 1.18 vol %, yielding nanospheres of steadily increasing diameter are shown. Pyrolyzation temperatures of (1) 600 °C, and (2) 900 °C do not significantly impact diameter. (b) Schematic of how sphere location and size impact the feasibility of successful APT tip. Tips A and B are preferred with top edges, while C and D demonstrate less desirable tips for APT. (c) STEM/EDS of two atom probe tips made under the same conditions demonstrate possible variability in sphere location with this technique.

ments on various processing steps are imperative to increase reliability and expand the information available from APT.

The following section discusses considerations that must be addressed when attempting to quantify APT results on materials such as N−C. The novelty of this technique has required optimization in many different areas, and these efforts are still continuing. Nevertheless, these initial advances show the promise of APT analysis for unprecedented characterization of soft nanomaterials.

Improving APT Reliability: Considerations for Future Experiments. *Particle Size Considerations.* The synthesized N−C_{sph} were chosen for this APT study due to their conveniently round morphology. While other morphologies of complex carbon materials could be analyzed using APT as well, the spherical shape allows for the reconstruction to be verified by having a spherical carbon sphere within the sample. Because of the low success rates and technical challenges to prepare APT tips that contain individual 50−100 nm particles, additional sets of N−C_{sph} were synthesized with larger diameters (Figure 5a). The full range of N−C_{sph} diameters reported by Wickramaratne allow for a variety of sizes to be synthesized.[55] Expected nanosphere sizes were confirmed from

https://dx.doi.org/10.1021/acsanm.9b02360
ACS Appl. Nano Mater. 2020, 3, 1600−1611

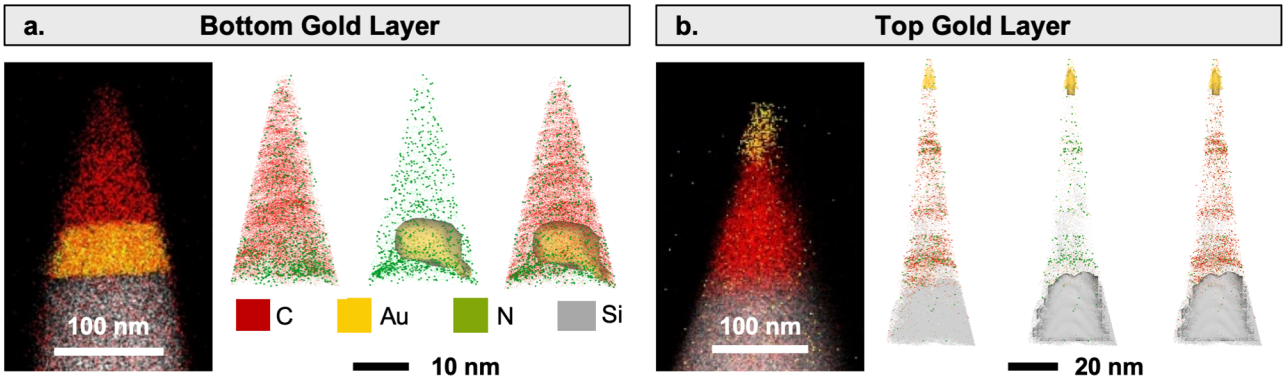

Figure 6. APT reconstructions and corresponding EDS maps of two N−C_{sph} tips with gold capping above and below sections of larger N−C_{sph}. Ideally, the C edge as denoted by Au coating is located near the top of the sharp tip. Reconstruction snapshots show (a) full point distribution for the listed elements (larger points for N in order to see distribution), iso surface for Au (0.4%), (b) full point distribution for C, N, Au iso surface (5%), and Si iso surface (20%). Reconstruction parameters can be found in the Supporting Information (Figures S6−S9).

TEM imaging (Figure S1), demonstrating close agreement with previously reported values of N−C_{sph} diameters. Here, we demonstrate that varying the pyrolyzation temperature does not change the size range of the particles, confirming that chemistry of the N−C_{sph} can be varied without impacting particle size (Figure 5a), making these samples suitable candidates for further APT studies. Series B (150−250 nm) is of particular interest to our APT work going forward, since medium diameter N−C_{sph} increase the success rate of producing viable APT samples that contain a particle of the N−C_{sph}, while also reducing time and effort spent locating an appropriate particle for encapsulation within a tip. However, increasing particle size comes with the trade-off of eliminating the possibility of capturing an entire particle within an APT tip (Figure 5b) which leaves only the bottom surface of the sphere to be analyzed. Owing to the lower probability of specimens surviving the analysis all the way through the bottom surface of the sphere and the likely increase in local trajectory aberration effects at that interface with this geometry, it is desirable to have an upper edge included (as seen in Figure 5b, tips A and B). Uncontrolled variation in preparation is demonstrated in Figure 5c, where tips were prepared from the same synthesis batch and under identical FIB conditions, yet are clearly different in shape and N−C_{sph} location. While this is a drawback, the 150−250 nm size range still enables the inclusion of both surface and bulk of an N−C_{sph} particle in a sharpened APT tip. Therefore, N−C_{sph} in Series B are highlighted in the remainder of this APT study, and the focus of our future work.

Sample Encapsulation Considerations. In addition to sample particle size, several external material conditions must be considered in order to isolate nanospheres into a workable APT tip. Particles must first be embedded into another material, in order to fill in air pockets formed between the sphere curvature and flat substrate. The surrounding matrix ideally has an evaporation field close to that of the sample, to avoid known aberrations in the reconstructed data which result from differences in the evaporation field.[65−67] The singularly high evaporation field of C (103 V/nm) is substantially greater than all known elements.

Although our initial work with Cu embedding was partially successful and inexpensive, its low evaporation field (30 V/nm) provides high likelihood for APT distortion from trajectory aberrations and premature evaporation (as discussed below with substrate considerations).[68] Elemental boron, the next-highest evaporation candidate (64 V/nm), does not naturally occur outside of small amounts in meteorites and is difficult to purify. Gold was identified as the most feasible option due to its higher evaporation field (53 V/nm) and accessibility as a commonly sputtered material, although with sputtering thickness limitations versus other metals. Subsequent samples for APT were prepared with Au sputtered above and below the spin-cast layer of N−C_{sph}. In addition to its function as a coating material, Au provides a high contrast marker for targeting N−C_{sph} in the FIB/SEM and for reference in APT reconstructions, improving the success rate of APT tip preparation and data analysis.

The coating material is crucial in nearly every step of the process: Locating N−C_{sph} during FIB/SEM, marking N−C_{sph} with STEM/EDS mapping, and subsequently as a reference for reconstructions. Once N−C_{sph} are isolated in the FIB, their precise geometries within the tip must be considered—specifically in order to capture both the surface and the bulk of a particle. Because gold should both coat nanosphere surfaces and comprise the layer on which particles sit, coatings provide more precise edge distinction. For such a ubiquitous material as carbon, the marker material also helps identify whether elemental signals originate from the targeted N−C or from contaminating external sources.

Ideally, Au will clearly mark a full circle/sphere (Figure 4a), however with larger diameter particles, only partial sections of a sphere's edges remain. For reconstruction accuracy of the larger spheres, a top C edge should be visible, as not only do tips lose sharpness with continued material removal down the sample, but also the bottom interface is more prone to fracture. When little to no gold remains on the top edge of the sphere, only the bottom edge remains clearly visible in the APT reconstruction (Figure 6a). To remedy this, alternate/improved methods to coat particles with thicker gold layers are under consideration.

Substrate Considerations. In addition to the external N−C coating, the substrate materials also require careful selection. Concerning both sample preparation and atom probe interpretation, various and often opposing properties must be considered: ease and rate of milling, resistance to evaporation, material cost, and possible mass interferences in the APT mass spectra. Softer semiconductors generally enhance the ease and precision of milling for FIB but are more likely to be removed from the tip prematurely (before higher evaporation field materials in the same spatial area) and thus misrepresented in

https://dx.doi.org/10.1021/acsanm.9b02360
ACS Appl. Nano Mater. 2020, 3, 1600−1611

reconstructions. Likewise, more robust materials provide higher APT accuracy while also providing more of a challenge during tip preparation.

During initial testing to attain appropriate tip morphology, thin silicon wafers were used for milling and cost efficiency. However, common silicon peaks (14 Da) overlap with that of nitrogen. Replacing Si with GaAs eliminates this overlapping peak issue, provides more straightforward substrate identification (due to the fact that Ga and As have definitive, isolated mass spectrum peaks, Table S5 and Figure S5), and allow for quicker sample preparation due to the material's relative softness. A caveat to GaAs is that the material also has a lower evaporation field, creating greater risk of out-of-sequence evaporation or delamination during atom probe operation. Subsequently, overall reconstruction accuracy is reduced with increased ease of substrate removal. While this does not affect quantification of other components, misplaced elements in reconstructions impair accuracy of 3D dopant distributions. FIB milling inherently implants Ga in any material; out-of-sequence substrate detection is thus indicated by the presence of arsenic species (not pictured) distributed through tips. A robust and reasonably priced alternative is a-plane sapphire, with the disadvantage of more difficult milling due to hardness and lack of electronic conductivity. Use of a sapphire substrate to replace gallium arsenide is a subject of future work.

Mass Spectra Considerations. Accurately identifying and interpreting the mass spectrum of any APT sample is imperative for reliable data, yet challenging for these samples. Many elements of similar mass exist in the low Dalton range where typical contaminants to the mass spectra are found, including O (16 Da), H_xO (17, 18, 19 Da), and CO_X (28, 44 Da), in variable quantities per sample (Figure SI 6). An additional complication for accurate quantification and reconstruction of these materials arises from the heteroatom of interest: nitrogen. Its main peaks (14, 28 Da) may overlap with the low-Da contaminant area discussed in Figure SI 7. Vast permutations exist when considering the effects of H (±1) and C (±6, 12, etc.) on detected ions, as well as external factors such as humidity. It is understood that omitting/including these compounds may decrease/increase the quantification of C/O in the actual sample, and thus change the relative amount of other identified compounds and subsequent single-element deconvolution. Crude quantification of the first sample (Figure 4) including these species produces high O values when normalized to C/O/N; including the low-Da species results in 53/45/2 atom % and C/N ratio of 23, whereas exclusion produces values much closer to those from EDS and XPS with 86/6/8 atom % and C/N of 10. This highlights the importance of correlating novel APT data with complementary techniques to improve confidence in the resulting data. The novelty of this technique limits the quantification from APT until preparation of comparable sample series and reconstructions are more reliably achieved. Individual regions of interest for each reconstruction may be selectively analyzed in order to isolate ambiguous and background peaks, helping determine if they originate from the $N-C_{sph}$ areas; this increases the confidence for omitting or including such peaks in final quantifications.

Reconstruction Reliability Considerations. Density discontinuities in reconstructions (Figure 6b) highlight the challenges of uneven evaporation and sample fracture during APT. Although $N-C_{sph}$ are nanoporous, the overall morphology should not have substantial discontinuities. Despite the fact that the data suggest an uneven distribution of nitrogen, the existence of similar gaps in the C distributions imply that the overall reconstructions are suffering from artifacts due to uneven evaporation. In general, the expected carbon distribution is homogeneous, as observed in the samples in Figure 6a and Figure 4, which both also demonstrate a relatively homogeneous distribution of nitrogen. Further down the tip, discontinuities appear in the Au layer beneath the $N-C_{sph}$, likely indicative of trajectory aberrations resulting from an irregular tip shape due to material fragmentation and uneven evaporation. Overall, while progress has been demonstrated, it is important to note that these techniques and data require further study before accurate commentary can be made on the precise dopant distribution. APT data can be [mis]represented in a myriad of ways. Here, Figures 4, 6a, and 6b are chosen to best approximate distributions based on the complementary characterization techniques. The techniques and the information acquired from them can be seen in Table 2.

Table 2. Complementary Information Obtained by Each Technique Featured in This Article[a]

characterization of functionalized carbon nanospheres			
technique	TEM/EDS	APT	XPS
information	2D image elemental structural	3D reconstruction elemental morphological	spectral elemental chemical
resolution	1 nm lateral	0.1−0.5 nm (3D)	10 μm lateral
surface sensitivity	N/A	N/A	1−10 nm
sample size	several nanospheres	single nanosphere	many nanospheres
sample prep	established	novel/challenging	established
data analysis	established	novel/challenging	established

[a]Multitechnique characterization allows for correlation between complementary information and different scales on the same material in order to better understand the complexities of functionalized carbon nanostructures.

In addition to the uncertainty of the flight trajectory and spatial assignment of elements with carbon materials, accurate mass spectrum ranging (peak identification) also contributes directly to the reliability of APT reconstruction. Although APT software provides spectral peak deconvolution methods that may be used to increase compositional accuracy, spatial resolution of the reconstruction is lost with this technique. Because of the methodological proof-of-concept intent of this publication, the APT data shown is preliminary, particularly since it is a known issue that standards and universally accepted methods do not exist to determine peak ranges. While the technique is capable of subnanometer resolution and tens of ppm compositional sensitivity depending on the material analyzed and analysis conditions, these carbon-based materials have not been verified to produce such results in a comprehensive manner. Attaining such an estimate of resolution requires standard samples with spatially identifiable features that can be used to validate the spatial accuracy of the reconstruction. Further work is necessary before more detailed analyses are warranted. Overall, the presented reconstructions are formulated such that the profiles most accurately represent the corresponding STEM/EDS data. It is suggested that further work on similar materials utilize multitechnique characterization in order to obtain the most reliable and

https://dx.doi.org/10.1021/acsanm.9b02360
ACS Appl. Nano Mater. 2020, 3, 1600−1611

complete data set. In Table 2, the techniques used are compared to demonstrate what information is determined from each technique, and why the multitechnique characterization was implemented to correlate uncertain APT data to alternate data acquired with XPS and TEM/EDS. In the interest of completeness, mass spectra for each APT are included in the Supporting Information (Figures S4−S9).

CONCLUSIONS

This study targeted a better understanding of variations in nitrogen distribution at the surface vs bulk for energy application materials and explored a path toward obtaining 3D atomic distributions of species within N-doped carbons using XPS, TEM, and APT. Keeping in mind challenges posed by APT sample prep and APT analysis, N−C_{sph} were synthesized with controlled size, shape, and composition, providing a sample set with varied chemical and physical properties relevant to various applications of this class of nanomaterials but also with dimensions that enable APT proof-of-principle. While no notable differences in the nitrogen distribution are detected with TEM/EDS, XPS analysis indicated variation in the distribution of nitrogen functionalities at different depths, motivating the development of an APT analysis method for this class of materials. A wealth of untapped information is potentially available through APT, including atomic distributions and clustering, both at the surface and within a bulk of material, which can provide invaluable information toward structure−property-performance correlations for this class of materials, yet it is still limited by several key issues that must be addressed. While uneven field evaporation, ambiguous/background peaks, and reconstruction accuracy are ongoing challenges for N−C_{sph} characterization by APT, our preliminary results show that analysis of carbon-based materials by APT is feasible and can provide insight on the dispersion of heteroatoms within a carbon matrix, complementing XPS and EDS analyses. Here, we provide a foundation for further study of functionalized C-based materials, which could be extended to even more complex energy application systems, such as C-based supports functionalized with more than one dopant, or catalysts with atomically dispersed transition metal(s) within the carbon or nitrogen-doped matrix, and other classes of complex functional nanomaterials.

ASSOCIATED CONTENT

Supporting Information

The Supporting Information is available free of charge at https://pubs.acs.org/doi/10.1021/acsanm.9b02360.

> Carbon sphere synthesis and characterization; N 1s peak assignment rationale and fitting parameters; FIB preparation considerations; cross correlation TEM images of APT tip; atom probe reconstruction parameters and mass spectra (PDF)

AUTHOR INFORMATION

Corresponding Author

Svitlana Pylypenko − *Department of Chemistry, Colorado School of Mines, Golden, Colorado 80401, United States;* orcid.org/0000-0001-7982-734X; Email: spylypen@mines.edu

Authors

Chilan Ngo − *Department of Chemistry, Colorado School of Mines, Golden, Colorado 80401, United States;* orcid.org/0000-0003-4084-098X

Margaret A. Fitzgerald − *Department of Chemistry, Colorado School of Mines, Golden, Colorado 80401, United States;* orcid.org/0000-0003-2976-0145

Michael J. Dzara − *Department of Chemistry, Colorado School of Mines, Golden, Colorado 80401, United States;* orcid.org/0000-0001-8125-0586

Matthew B Strand − *Department of Chemistry, Colorado School of Mines, Golden, Colorado 80401, United States;* orcid.org/0000-0001-8810-1743

David R. Diercks − *Department of Metallurgical and Materials Engineering, Colorado School of Mines, Golden, Colorado 80401, United States;* orcid.org/0000-0002-5138-0168

Complete contact information is available at: https://pubs.acs.org/10.1021/acsanm.9b02360

Author Contributions

#These authors contributed equally to this work.

Notes

The authors declare no competing financial interest.

ACKNOWLEDGMENTS

This work was supported by start-up funds from Colorado School of Mines and NSF Award No. 1800585 Probing Catalyst−Support Interactions via Experiment and Theory. This research used resources of the Advanced Light Source, which is a DOE Office of Science User Facility under Contract No. DE-AC02-05CH11231. The authors also acknowledge resources and support from the Electron Microscopy user facility at the Colorado School of Mines.

REFERENCES

(1) Donnet, J.-B. Fifty Years of Research and Progress on Carbon Black. *Carbon* **1994**, *32* (7), 1305−1310.

(2) Wang, C. Z.; Ho, K. M. Structure, Dynamics, and Electronic Properties of Diamondlike Amorphous Carbon. *Phys. Rev. Lett.* **1993**, *71* (8), 1184−1187.

(3) Chand, S. Carbon Fibers for Composites. *J. Mater. Sci.* **2000**, *35* (35), 1303−1313.

(4) Lee, J.; Kim, J.; Hyeon, T. Recent Progress in the Synthesis of Porous Carbon Materials. *Adv. Mater.* **2006**, *18*, 2073−2094.

(5) Solis-Fernandez, P.; Bissett, M.; Ago, H. Synthesis, Structure and Applications of Graphene-Based 2D Heterostructures. *Chem. Soc. Rev.* **2017**, *46*, 4572−4613.

(6) Thostenson, E. T.; Ren, Z.; Chou, T. Advances in the Science and Technology of Carbon Nanotubes and Their Composites: A Review. *Compos. Sci. Technol.* **2001**, *61*, 1899−1912.

(7) Wood, K. N.; O'Hayre, R.; Pylypenko, S. Recent Progress on Nitrogen/Carbon Structures Designed for Use in Energy and Sustainability Applications. *Energy Environ. Sci.* **2014**, *7*, 1212−1249.

(8) Paraknowitsch, J. P.; Thomas, A. Doping Carbons beyond Nitrogen: An Overview of Advanced Heteroatom Doped Carbons with Boron, Sulphur and Phosphorus for Energy Applications. *Energy Environ. Sci.* **2013**, *6*, 2839−2855.

(9) Fischer, J. E. Chemical Doping of Single-Wall Carbon Nanotubes. *Acc. Chem. Res.* **2002**, *35* (12), 1079−1086.

(10) Stoyanov, S. R.; Titov, A. V.; Král, P. Transition Metal and Nitrogen Doped Carbon Nanostructures. *Coord. Chem. Rev.* **2009**, *253*, 2852−2871.

(11) Xia, Y.; Zhu, Y.; Tang, Y. Preparation of Sulfur-Doped Microporous Carbons for the Storage of Hydrogen and Carbon Dioxide. *Carbon* **2012**, *50*, 5543−5553.

(12) Bult, J. B.; Lee, J.; O'Neill, K.; Engtrakul, C.; Hurst, K. E.; Zhao, Y.; Simpson, L. J.; Parilla, P. A.; Gennett, T.; Blackburn, J. L. Manipulation of Hydrogen Binding Energy and Desorption Kinetics by Boron Doping of High Surface Area Carbon. *J. Phys. Chem. C* **2012**, *116*, 26138−26143.
(13) Yang, D.-S.; Bhattacharjya, D.; Inamdar, S.; Park, J.; Yu, J.-S. Phosphorus-Doped Ordered Mesoporous Carbons with Different Lengths as Efficient Metal-Free Electrocatalysts for Oxygen Reduction Reaction in Alkaline Media. *J. Am. Chem. Soc.* **2012**, *134*, 16127−16130.
(14) Cao, Y.; Yu, H.; Tan, J.; Peng, F.; Wang, H.; Li, J.; Zheng, W.; Wong, N.-B. Nitrogen-, Phosphorous- and Boron-Doped Carbon Nanotubes Catalysts for the Aerobic Oxidation of Cyclohexane. *Carbon* **2013**, *57*, 433−442.
(15) Pylypenko, S.; Borisevich, A.; More, K. L.; Corpuz, A. R.; Holme, T.; Dameron, A. A.; Olson, T. S.; Dinh, H. N.; Gennett, T.; O'Hayre, R. Nitrogen: Unraveling the Secret to Stable Carbon-Supported Pt-Alloy Electrocatalysts. *Energy Environ. Sci.* **2013**, *6*, 2957−2964.
(16) Stambula, S.; Gauquelin, N.; Bugnet, M.; Gorantla, S.; Turner, S.; Sun, S.; Liu, J.; Zhang, G.; Sun, X.; Botton, G. A. Chemical Structure of Nitrogen-Doped Graphene with Single Platinum Atoms and Atomic Clusters as a Platform for the PEMFC Electrode. *J. Phys. Chem. C* **2014**, *118*, 3890−3900.
(17) Guo, J.; Yang, Z.; Yu, Y.; Abruna, H. D.; Archer, L. A. Lithium-Sulfur Battery Cathode Enabled by Lithium-Nitrile Interaction. *J. Am. Chem. Soc.* **2013**, *135*, 763−767.
(18) Ozaki, J.; Kimura, N.; Anahara, T.; Oya, A. Preparation and Oxygen Reduction Activity of BN-Doped Carbons. *Carbon* **2007**, *45*, 1847−1853.
(19) Kim, J.; Han, J.; Ha, D.; Kang, S. Synthesis of Nitrogen and Boron Co-Doped Carbon (CNB) and Their CO_2 Capture Properties: From Porous to Hollow Granule Structure. *J. Mater. Chem. A* **2014**, *2*, 16645−16651.
(20) Wang, Y.; Qiao, J.; Baker, R.; Zhang, J. Alkaline Polymer Electrolyte Membranes for Fuel Cell Applications. *Chem. Soc. Rev.* **2013**, *42*, 5768−5787.
(21) Yang, S.; Peng, L.; Huang, P.; Wang, X.; Sun, Y.; Cao, C.; Song, W. Nitrogen, Phosphorus, and Sulfur Co-Doped Hollow Carbon Shell as Superior Metal-Free Catalyst for Selective Oxidation of Aromatic Alkanes. *Angew. Chem., Int. Ed.* **2016**, *55*, 4016−4020.
(22) Matter, P. H.; Zhang, L.; Ozkan, U. S. The Role of Nanostructure in Nitrogen-Containing Carbon Catalysts for the Oxygen Reduction Reaction. *J. Catal.* **2006**, *239* (1), 83−96.
(23) Wu, G.; More, K. L.; Johnston, C. M.; Zelenay, P. High-Performance Electrocatalysts for Oxygen Reduction Derived from Polyaniline, Iron, and Cobalt. *Science (Washington, DC, U. S.)* **2011**, *332*, 443−448.
(24) Workman, M. J.; Dzara, M. J.; Ngo, C.; Pylypenko, S.; Serov, A.; McKinney, S.; Gordon, J.; Atanassov, P.; Artyushkova, K. Platinum Group Metal-Free Electrocatalysts: Effects of Synthesis on Structure and Performance in Proton-Exchange Membrane Fuel Cell Cathodes. *J. Power Sources* **2017**, *348*, 30−39.
(25) Kruusenberg, I.; Ramani, D.; Ratso, S.; Joost, U.; Saar, R.; Rauwel, P.; Kannan, A. M.; Tammeveski, K. Cobalt-Nitrogen Co-Doped Carbon Nanotube Cathode Catalyst for Alkaline Membrane Fuel Cells. *ChemElectroChem* **2016**, *3* (9), 1455−1465.
(26) Joglekar, M.; Pylypenko, S.; Otting, M. M.; Valenstein, J. S.; Trewyn, B. G. Universal and Versatile Route for Selective Covalent Tethering of Single-Site Catalysts and Functional Groups on the Surface of Ordered Mesoporous Carbons. *Chem. Mater.* **2014**, *26*, 2873−2882.
(27) Ren, W.-M.; Liu, Z.-W.; Wen, Y.-Q.; Zhang, R.; Lu, X. Mechanistic Aspects of the Copolymerization of CO_2 with Epoxides Using a Thermally Stable Single-Site Cobalt (III) Catalyst. *J. Am. Chem. Soc.* **2009**, *131*, 11509−11518.
(28) Pan, Y.; Lin, R.; Chen, Y.; Liu, S.; Zhu, W.; Cao, X.; Chen, W.; Wu, K.; Cheong, W.-C.; Wang, Y.; Zheng, L.; Luo, J.; Lin, Y.; Liu, Y.; Liu, C.; Li, J.; Lu, Q.; Chen, X.; Wang, D.; Peng, Q.; Chen, C.; Li, Y. Design of Single-Atom Co-N_5 Catalytic Site: A Robust Electrocatalyst for CO_2 Reduction with Nearly 100% CO Selectivity and Remarkable Stability. *J. Am. Chem. Soc.* **2018**, *140*, 4218−4221.
(29) Wohlgemuth, S.-A.; White, R. J.; Willinger, M.-G.; Titirici, M.-M.; Antonietti, M. A One-Pot Hydrothermal Synthesis of Sulfur and Nitrogen Doped Carbon Aerogels with Enhanced Electrocatalytic Activity in the Oxygen Reduction Reaction. *Green Chem.* **2012**, *14*, 1515−1523.
(30) Sharifi, T.; Hu, G.; Jia, X.; Wågberg, T. Formation of Active Sites for Oxygen Reduction Reactions by Transformation of Nitrogen Functionalities in Nitrogen-Doped Carbon Nanotubes. *ACS Nano* **2012**, *6* (10), 8904−8912.
(31) Li, W.; Zhou, M.; Li, H.; Wang, K.; Cheng, S.; Jiang, K. A High Performance Sulfur-Doped Disordered Carbon Anode for Sodium Ion Batteries. *Energy Environ. Sci.* **2015**, *8*, 2916−2921.
(32) Yang, L.; Jiang, S.; Zhao, Y.; Zhu, L.; Chen, S.; Wang, X.; Wu, Q.; Ma, J.; Ma, Y.; Hu, Z. Boron-Doped Carbon Nanotubes as Metal-Free Electrocatalysts for the Oxygen Reduction Reaction. *Angew. Chem.* **2011**, *123*, 7270−7273.
(33) Wood, K. N.; Pylypenko, S.; Olson, T. S.; Dameron, A. A.; O'Neill, K.; Christensen, S. T.; Dinh, H. N.; Gennett, T.; O'Hayre, R. Effect of Halide-Modified Model Carbon Supports on Catalyst Stability. *ACS Appl. Mater. Interfaces* **2012**, *4* (12), 6728−6734.
(34) Guo, D.; Shibuya, R.; Akiba, C.; Saji, S.; Kondo, T.; Nakamura, J. Active Sites of Nitrogen-Doped Carbon Materials for Oxygen Reduction Reaction Clarified Using Model Catalysts. *Science (Washington, DC, U. S.)* **2016**, *351* (6271), 361−365.
(35) Pylypenko, S.; Queen, A.; Olson, T. S.; Dameron, A.; O'Neill, K.; Neyerlin, K. C.; Pivovar, B.; Dinh, H. N.; Ginley, D. S.; Gennett, T.; O'Hayre, R. Tuning Carbon-Based Fuel Cell Catalyst Support Structures via Nitrogen Functionalization. I., Investigation of Structural and Compositional Modification of Highly Oriented Pyrolytic Graphite Model Catalyst Supports as a Function of Nitrogen Implantation Dose. *J. Phys. Chem. C* **2011**, *115*, 13667−13675.
(36) Belin, T.; Epron, F. Characterization Methods of Carbon Nanotubes: A Review. *Mater. Sci. Eng., B* **2005**, *119*, 105−118.
(37) Müller, E. W.; Panitz, J. A.; McLane, S. B. The Atom-Probe Field Ion Microscope. *Rev. Sci. Instrum.* **1968**, *39*, 83−86.
(38) Devaraj, A.; Perea, D. E.; Liu, J.; Gordon, L. M.; Prosa, T. J.; Diercks, D. R.; Meher, S.; Kolli, R. P.; Meng, Y. S.; Thevuthasan, S. Three-Dimensional Nanoscale Characterisation of Materials by Atom Probe Tomography. *Int. Mater. Rev.* **2018**, *63* (2), 68−101.
(39) Felfer, P.; Benndorf, P.; Masters, A.; Maschmeyer, T.; Cairney, J. M. Revealing the Distribution of the Atoms within Individual Bimetallic Catalyst Nanoparticles. *Angew. Chem.* **2014**, *126*, 11372−11375.
(40) Proudian, A. P.; Jaskot, M. B.; Lyiza, C.; Diercks, D. R.; Gorman, B. P.; Zimmerman, J. D. Effect of Diels-Alder Reaction in C_{60}-Tetracene Photovoltaic Devices. *Nano Lett.* **2016**, *16*, 6086−6091.
(41) Perea, D. E.; Hemesath, E. R.; Schwalbach, E. J.; Lensch-Falk, J. L.; Voorhees, P. W.; Lauhon, L. J. Direct Measurement of Dopant Distribution in an Individual Vapour-Liquid-Solid Nanowire. *Nat. Nanotechnol.* **2009**, *4*, 315−319.
(42) Diercks, D. R.; Gorman, B. P.; Kirchhofer, R.; Sanford, N.; Bertness, K.; Brubaker, M. Atom Probe Tomography Evaporation Behavior of C-Axis GaN Nanowires: Crystallographic, Stoichiometric, and Detection Efficiency Aspects. *J. Appl. Phys.* **2013**, *114*, 184903.
(43) Du, S.; Burgess, T.; Gault, B.; Gao, Q.; Bao, P.; Li, L.; Cui, X.; Yeoh, W. K.; Liu, H.; Yao, L.; Ceguerra, A. V.; Tan, H. H.; Jagadish, C.; Ringer, S.; Zheng, R. Quantitative Dopant Distributions in GaAs Nanowires Using Atom Probe Tomography. *Ultramicroscopy* **2013**, *132*, 186−192.
(44) Diercks, D. R.; Gorman, B. P.; Manerbino, A.; Coors, G. Atom Probe Tomography of Yttrium-Doped Barium-Cerium-Zirconium Oxide with NiO Addition. *J. Am. Ceram. Soc.* **2014**, *97* (10), 3301−3306.

https://dx.doi.org/10.1021/acsanm.9b02360
ACS Appl. Nano Mater. 2020, 3, 1600−1611

(45) Devaraj, A.; Vijayakumar, M.; Bao, J.; Guo, M. F.; Derewinski, M. A.; Xu, Z.; Gray, M. J.; Prodinger, S.; Ramasamy, K. K. Discerning the Location and Nature of Coke Deposition from Surface to Bulk of Spent Zeolite Catalysts. *Sci. Rep.* **2016**, *6*, 1−11.
(46) Schmidt, J. E.; Oord, R.; Guo, W.; Poplawsky, J. D.; Weckhuysen, B. M. Nanoscale Tomography Reveals the Deactivation of Automotive Copper-Exchanged Zeolite Catalysts. *Nat. Commun.* **2017**, *8* (1666), 1−8.
(47) Larson, D. J.; Giddings, A. D.; Wu, Y.; Verheijen, M. A.; Roozeboom, F.; Rice, K. P.; Kessels, W. M. M.; Geiser, B. P.; Kelly, T. F. Encapsulation Method for Atom Probe Tomography Analysis of Nanoparticles. *Ultramicroscopy* **2015**, *159* (2), 420−426.
(48) Felfer, P.; Li, T.; Eder, K.; Galinski, H.; Magyar, A. P.; Bell, D. C.; Smith, G. D. W.; Kruse, N.; Ringer, S. P.; Cairney, J. M. New Approaches to Nanoparticle Sample Fabrication for Atom Probe Tomography. *Ultramicroscopy* **2015**, *159* (2), 413−419.
(49) Li, T.; Bagot, P. A. J.; Christian, E.; Theobald, B. R. C.; Sharman, J. D. B.; Ozkaya, D.; Moody, M. P.; Tsang, S. C. E.; Smith, G. D. W. Atomic Imaging of Carbon-Supported Pt, Pt/Co, and Ir@Pt Nanocatalysts by Atom-Probe Tomography. *ACS Catal.* **2014**, *4* (2), 695−702.
(50) Heck, P. R.; Stadermann, F. J.; Isheim, D.; Auciello, O.; Daulton, T. L.; Davis, A. M.; Elam, J. W.; Floss, C.; Hiller, J. M.; Larson, D. J.; Lewis, J. B.; Mane, A. U.; Pellin, M. J.; Savina, M. R.; Seidman, D. N.; Stephan, T. G. Atom-Probe Analyses of Nanodiamonds from Allende. *Meteorit. Planet. Sci.* **2014**, *49* (3), 453−467.
(51) Diercks, D. R.; Gorman, B. P.; Cheung, C. L.; Wang, G. Techniques for Consecutive TEM and Atom Probe Tomography Analysis of Nanowires. *Microsc. Microanal.* **2009**, *15* (2), 254−255.
(52) Sun, Z.; Hazut, O.; Yerushalmi, R.; Lauhon, L. J.; Seidman, D. N. Criteria and Considerations for Preparing Atom-Probe Tomography Specimens of Nanomaterials Utilizing an Encapsulation Methodology. *Ultramicroscopy* **2018**, *184*, 225−233.
(53) Briggs, D.; Seah, M. P. *Practical Surface Analysis, Auger and X-Ray Photoelectron Spectroscopy*; Practical Surface Analysis; Wiley, 1996.
(54) Jablonski, A.; Powell, C. Relationships between Electron Inelastic Mean Free Paths, Effective Attenuation Lengths, and Mean Escape Depths. *J. Electron Spectrosc. Relat. Phenom.* **1999**, *100* (1−3), 137−160.
(55) Wickramaratne, N. P.; Xu, J.; Wang, M.; Zhu, L.; Dai, L.; Jaroniec, M. Nitrogen Enriched Porous Carbon Spheres: Attractive Materials for Supercapacitor Electrodes and CO_2 Adsorption. *Chem. Mater.* **2014**, *26*, 2820−2828.
(56) Grass, M. E.; Karlsson, P. G.; Aksoy, F.; Lundqvist, M.; Wannberg, B.; Mun, B. S.; Hussain, Z.; Liu, Z. New Ambient Pressure Photoemission Endstation at Advanced Light Source Beamline 9.3.2. *Rev. Sci. Instrum.* **2010**, *81*, 053106.
(57) Gorman, B. P.; Diercks, D.; Salmon, N.; Stach, E.; Amador, G.; Hartfield, C. Hardware and Techniques for Cross-Correlative TEM and Atom Probe Analysis. *Microsc. Today* **2008**, *16*, 42−47.
(58) Ferrandon, M.; Kropf, J. A.; Myers, D. J.; Kramm, U.; Bogdanoff, P.; Wu, G.; Johnston, C. M.; Zelenay, P. Multitechnique Characterization of a Polyaniline - Iron - Carbon Oxygen Reduction Catalyst. *J. Phys. Chem. C* **2012**, *116*, 16001−16013.
(59) Dzara, M. J.; Artyushkova, K.; Shulda, S.; Strand, M. B.; Ngo, C.; Crumlin, E. J.; Gennett, T.; Pylypenko, S. Characterization of Complex Interactions at the Gas - Solid Interface with in Situ Spectroscopy: The Case of Nitrogen-Functionalized Carbon. *J. Phys. Chem. C* **2019**, *123* (14), 9074−9086.
(60) Matanovic, I.; Artyushkova, K.; Strand, M. B.; Dzara, M. J.; Pylypenko, S.; Atanassov, P. Core Level Shifts of Hydrogenated Pyridinic and Pyrrolic Nitrogen in the Nitrogen-Containing Graphene-Based Electrocatalysts: In-Plane vs Edge Defects. *J. Phys. Chem. C* **2016**, *120*, 29225−29232.
(61) Wood, K. N.; Christensen, S. T.; Nordlund, D.; Dameron, A. A.; Ngo, C.; Dinh, H.; Gennett, T.; O'Hayre, R.; Pylypenko, S. Spectroscopic Investigation of Nitrogen-Functionalized Carbon Materials. *Surf. Interface Anal.* **2016**, *48*, 283−292.
(62) Artyushkova, K.; Kiefer, B.; Halevi, B.; Knop-Gericke, A.; Schlogl, R.; Atanassov, P. Density Functional Theory Calculations of XPS Binding Energy Shift for Nitrogen-Containing Graphene-like Structures. *Chem. Commun.* **2013**, *49*, 2539−2541.
(63) Arslan, I.; Marquis, E. A.; Homer, M.; Hekmaty, M. A.; Bartelt, N. C. Towards Better 3-D Reconstructions by Combining Electron Tomography and Atom-Probe Tomography. *Ultramicroscopy* **2008**, *108*, 1579−1585.
(64) Vurpillot, F.; Gault, B.; Geiser, B. P.; Larson, D. J. Reconstructing Atom Probe Data: A Review. *Ultramicroscopy* **2013**, *132*, 19−30.
(65) Larson, D. J.; Geiser, B. P.; Prosa, T. J.; Gertsl, S. S. A.; Reinhard, D. A.; Kelly, T. F. Improvements in Planar Feature Reconstructions in Atom Probe Tomography. *J. Microsc.* **2011**, *243* (1), 15−30.
(66) Vurpillot, F.; Larson, D.; Cerezo, A. Improvement of Multilayer Analyses with a Three-Dimensional Atom Probe. *Surf. Interface Anal.* **2004**, *36*, 552−558.
(67) Marquis, E. A.; Vurpillot, F. Chromatic Aberrations in the Field Evaporation Behavior of Small Precipitates. *Microsc. Microanal.* **2008**, *14* (6), 561−570.
(68) Miller, M. K.; Cerezo, A.; Hetherington, M. G.; Smith, G. D. W. *Atom Probe Field Ion Microscopy*; Oxford Science Publications, 1996.

https://dx.doi.org/10.1021/acsanm.9b02360
ACS Appl. Nano Mater. 2020, 3, 1600−1611